

First-principles based Monte Carlo modeling of oxygen deficient Fe-substituted SrTiO₃ experimental magnetization

Juan M. Florez^a, Miguel A. Solis^a, Emilio A. Cortés Estay^a, E. Suárez Morell^{a,b}, Caroline A. Ross^c

^a*Grupo de Simulaciones, Departamento de Física, Universidad Técnica Federico Santa María, Valparaíso 2390123, Chile*

^b*Departamento de Física Aplicada I, Escuela Politécnica Superior, Universidad de Sevilla, España*

^c*Department of Materials Science and Engineering, Massachusetts Institute of Technology, Cambridge, MA 02139, USA*

Abstract

Ferroics based on transition-metal (TM) substituted SrTiO₃ have called much attention as magnetism and/or ferroelectricity can be tuned by using cations substitution and defects, strain and/or oxygen deficiency. C. A. Ross et al. [Phys. Rev. Applied 7, 024006 (2017)] demonstrated the SrTi_{1-x}Fe_xO_{3-δ} (STF) magnetization behavior for different deposition oxygen-pressures, substrates and magnetic fields. The relation between oxygen deficiency and ferroic orders is yet to be well understood, for which the full potential of oxygen-stoichiometry engineered materials remain an open question. Here, we use hybrid-DFT to calculate different oxygen vacancy (v_o) states in STF with a variety of TM distributions. The resulting cations' magnetic states and alignments associated to the v_o ground-states for $x = \{0.125, 0.25\}$ are used within a Monte Carlo scope for collinear magnetism to simulate the spontaneous magnetization. Our model captures several experimental STF features i.e., display a maximum of the magnetization at intermediate number of vacancies, a monotonous quenching from $\sim 0.35\mu_B$ for small δ , and a slower decreasing of such saturation for larger number of vacancies. Moreover, our approach gives a further insight into the relations between defects stabilization and magnetization, vacancy density and the oxygen pressure required to maximize such ferroic order, and sets guidelines for future Machine Learning based computational synthesis of multiferroic oxides.

Keywords: magnetic perovskites, Monte Carlo, oxygen deficiency, density functional theory

1. Introduction

Perovskite-structured oxides exhibit an exceptionally rich variety of electronic properties including ferroelectricity [1, 2, 3, 4], magnetic order, superconductivity [5, 6, 7, 8], and multiferroicity [9, 10, 11], properties that can be tuned via the composition, doping, strain state, and defect population of the material [10, 12, 13, 14, 15, 16, 17, 18]. One of the cornerstones of oxide electronics is SrTiO₃ (STO) which has a large bandgap and nonmagnetic behavior at room temperature [19]. STO can be integrated with Si devices, and ferroelectric and magnetic behavior can be promoted by strain and by magnetic substitution, respectively [9, 10, 18, 19, 20]. Recent work has focused

on the role of oxygen-defects and introduction of Ti-substituent on the multiferroic properties [10, 13, 14, 15, 16, 17, 18, 20, 21, 22, 23, 24, 25, 26, 27, 28], and an interplay between the oxygen stoichiometry and the magnetic and ferroelectric degrees of freedom has been demonstrated.

Stoichiometry in ABO₃ perovskites was thought to be a key to obtain robust magnetization [29], and the introduction of oxygen vacancies (v_O) or cation defects usually led to weak magnetic ordering or paramagnetic-like states [10, 30]. However, experimental results have shown that O-deficiency is capable of turning a magnetic semimetal such as SrCoO₃ (SCO) into a semiconductor as well as converting the insulating paramagnetic STO into a magnetic semiconductor or weak ferroelectric [9, 20, 31]. $3d$ -orbitals in transition metal (TM) cations are distorted by incomplete oxygen octahedral coordination O_{5,4}, and both the covalent

Email address:

caross@mit.edu, juanmanuel.florez@usm.cl (Juan M. Florez)

Preprint submitted to Journal of L^AT_EX Templates

February 24, 2023

and ionic bondings characters through O-A/B- v_O defects plays a relevant role [32], as in the case of the multi-interpreted SCO spin-states [31] and the magnetism in Fe,Co-substituted STO[33, 34].

On the other hand, ferroic ordering can be engineered through defects in ABO_3 perovskites, e.g. at low temperatures, stoichiometric STO presents antiferrodistortive structural changes and quantum fluctuations that suppress the ferroelectric (FE) ordering [35, 36]. Also, coupling of interstitial and anti-site Ti with Sr and O vacancies, have been suggested to promote polar effects beside magnetism [37, 38, 39, 40, 41, 42]. Multiferroism in oxygen deficient $SrFeO_3$ nanoparticles was studied [43] and it displayed saturation electric-polarization depending on the Fe concentration [27]. Moreover, electric polarization was realized in magnetic Fe-doped Ti-rich STO at room temperature[44]. Among TM-substituted STO, $SrTi_{1-x}Fe_xO_{3-\delta}$ (STF) and $SrTi_{1-x}Co_xO_{3-\delta}$ (STC) both display magnetization that depends on their oxygen content, with typically higher magnetization at higher levels of oxygen deficiency (δ), and a distinct magnetization maxima characterizing STF [10, 31, 45].

In this work, we focus on the magnetic properties of STF. Its magnetic properties can be varied via both cation composition and O deficiency. Moreover, room temperature magnetism and anisotropy with out-of-plane magnetic easy axis are observed in thin films of nondilute STF and STC deposited on different substrates, showing that both strain and oxygen deficiency are key factors in determining the magnetic properties of substituted STO, and the effect of oxygen pressure during growth has also been explored [10, 31]. The magnetization of STC and STF increases with the Co or Fe content, and is higher for lower growth pressure and therefore greater oxygen vacancy concentration, although for STF a decrease in magnetization was found at the lowest growth pressures [10, 30, 31, 46, 47, 48]. Using XMCD we showed that the magnetic moment in STF was proportional to the concentration of divalent Fe which increased on films grown at low pressures or annealed in a reducing environment [10, 30]. The magnetic properties are intrinsically tied to the allowed mixture of valence and spin states and the corresponding ferromagnetic (FM) or antiferromagnetic (AFM) local spin-ordering,

which strongly depends upon the oxygen vacancies coordinating the transition metal ions.

A comprehensive model of the perovskite vacancies distribution and its repercussion with respect to the ferroic order parameters remains a challenge. Moreover, in STF, experimental magnetization can not be completely interpreted as a direct consequence of the changes in the cations valence spin states and TM symmetry alone [10, 30], for which the distinction between different vacancy stabilized local spin orderings and breaking of symmetry should be taken into account in a wider way next. We theoretically investigate the spontaneous/saturation magnetization of STF. First, we use hybrid-DFT methods to obtain the STF spin-states, local magnetic ordering, and energetically favored TM symmetry and defects formation; then use that microscopic information to feed an intuitive statistical model for the magnetization observable, whose probability distribution is calculated by using a Monte Carlo method that samples over the vacancies configurations space for any given number of vacancies, while the symmetry and magnetic constrictions imposed by the ground state solutions conforming such configurations are fulfilled. STF magnetization maximization result for an intermediate oxygen pressure has not been addressed either partly because of the difficulty in terms of the large configurational space to be considered besides the variety of thermodynamic and chemical-physicist conditions related to the deposition and synthesis. Our microscopic and statistical approaches both are to a good extent in agreement with STF experiments and might apply to other ABO_3 systems.

This article is organized as follows: In section 2 we introduce the perovskite model, the DFT methods, and the MC approach. In section 3 we show the DFT results for stoichiometric and oxygen deficient systems with $\delta = \{0, 0.125\}$, and $x = \{0.125, 0.25\}$. In section 4 we present the MC statistical analysis for the STF magnetization. In section 5 the conclusions are presented.

2. Modeling framework

We use density functional theory with a Heyd-Scuseria-Ernzerhof (HSE06) exchange-correlation functional as implemented in the Vienna Abinitio Simulation Package (VASP 5.4) [49, 50, 51] to

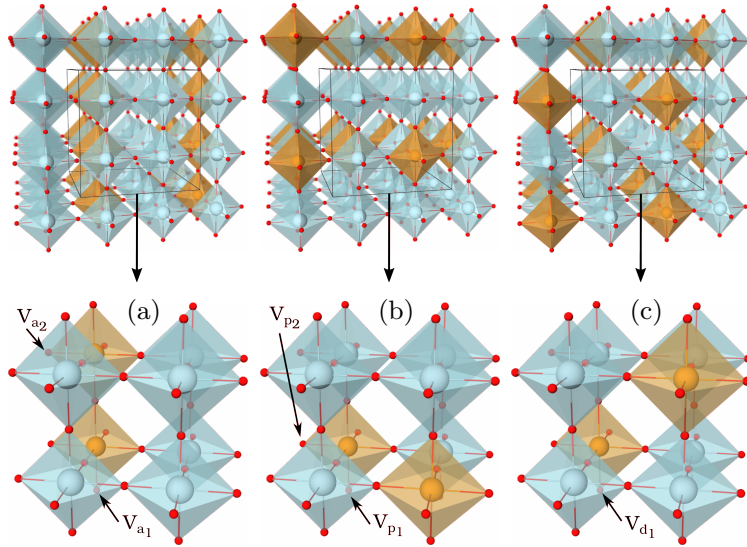


Figure 1: Supercell for $x = 0.25$ in $\text{SrTi}_{1-x}\text{Fe}_x\text{O}_{3-\delta}$: (a) Fe-Fe pair with $nn_{\text{Fe}} = a$. (b) Fe-Fe pair with $nn_{\text{Fe}} = a\sqrt{2}$; and (c) Fe-Fe pair with $nn_{\text{Fe}} = a\sqrt{3}$. a is initially the STO lattice parameter. The vacancies are depicted as: $V_{a1,2}$, $V_{p1,2}$ and V_{d1} , respectively. The Sr atoms have been omitted for the sake of simplicity. Graphical representations were produced using the OVITO software [66].

study the effects of oxygen deficiency in STF. The use of a hybrid functional leads to improved accuracy over standard local and semi-local functionals such as LSDA, GGA or Perdew-Burke-Ernzerhof (PBE) for predictions of key properties such as valence spin-states, chemical-induced structural changes and band-gaps in 3d-oxides as shown previously e.g., for SCO, STO, STC and $\text{SrTi}_{1-x-y}\text{Fe}_x\text{Co}_y\text{O}_{3-\delta}$ (STFC) [10, 33, 31]. We also performed GGA+U calculations in order to examine the stability of selected Fe spin-states under strain for the sake of discussion, because HSE06 functional incurs in large computational costs compared to local methods.

The spin-polarized calculations were performed with an energy cutoff of 500 eV for $2 \times 2 \times 2$ and $4 \times 4 \times 4$ k-point grids in the case of HSE06, for relaxations and static calculations, respectively, and $6 \times 6 \times 6$ for GGA+U in both cases. The HSE06 grids were chosen to keep the computational costs at a reasonable level, and the results represent converged relaxations with forces below 10^{-4} eV/Å. Our screening value μ was chosen similar to References [10, 31] to compare with STC/STO results, and the $U_{eff} = U - J$ terms were used within Dudarev's GGA+U approach for the d -Fe electrons [52]. In the latter case, the acting forces were reduced below 10^{-5} eV/Å, and the U_{eff} values were

chosen within the range of validity of recent simulations for STFC i.e., 4 and 7 eV for 3d-orbitals were applied to Fe and Ti, respectively [34]. In the case of the ab-initio calculations, the supercell of the solid solutions consisted of $2 \times 2 \times 2$ unit cells with $\{40, 39\}$ ions for $\delta = \{0.0, 0.125\}$, as displayed in Figure 1. PBE pseudopotentials were used with $3s^2 4p^6 5s^2$, $3d^3 4s^1$, $3d^7 4s^1$, and $2s^2 2p^4$ distributions for Sr, Ti, Fe, and O respectively.

The positions of the oxygen vacancies, shown in lower panels of Figure 1 as $V_{a,p,d(1,2)}$, were selected after a symmetry analysis of the relaxed stoichiometric systems corresponding to three different distributions of the Fe cations within the supercells for %25 Fe substitution, obtained with FINDSYM and pymatgen applications [53, 54, 55] for a 10^{-3} Å tolerance. The Fe-nearest-neighbor (nn) distances considered were $\{a, \sqrt{2}a, \sqrt{3}a\}$, with a the initial unit-cell parameter. According to each configuration, we have considered all the atomic valence states, which are reflected in several possible high and low Pauli states for the TM, as well as the possible combinations for the FM or AFM Fe-Fe exchange coupling. The valences of the cations are selected to maintain a neutral supercell for a given oxygen deficiency, and point/bulk-charging effects due to these defects are negligible as suggested by DFT calculations in STF and STFC [33, 34]. We

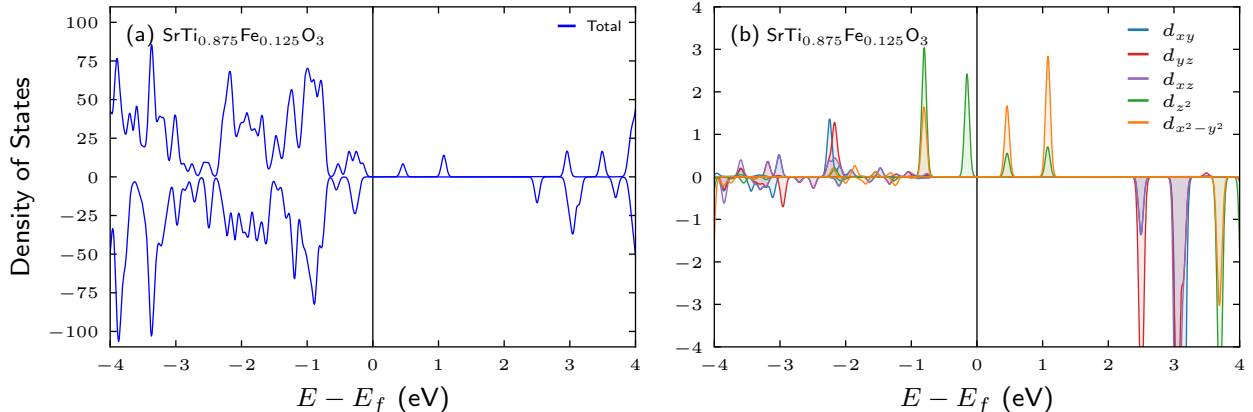


Figure 2: (a) Total Density of States (DOS) and (b) Fe ion d -orbitals projected DOS for $\text{SrTi}_{0.875}\text{Fe}_{0.125}\text{O}_3$.

also refer in this work, without loss of generality, to $V_{a,p,d(1,2)}$ as the vacancies corresponding to the Fe cations aligned along the $[1, 0, 0]$ (above), $[1, 1, 0]$ (plane) and $[1, 1, 1]$ (diagonal) crystalline directions, respectively.

To model the magnetic order parameter we use Monte Carlo (MC) [56] calculations to extract v_{O} -configurational probabilities for specific cations distributions and using $4 \times 4 \times 4$ supercells as displayed in the upper panels of Figure 1. Within a Metropolis [57] scheme an algorithm with an aleatory-sampling acceptance $\text{rand}(0, 1) \leq \exp(-\Delta E/k_B T)$ is implemented. Here the ΔE energies are obtained from ab-initio characterization, such that they discriminate the states corresponding to FM from the AFM ones, as well as the lowest-energy states (gs) from second to lowest solutions (ss), for a representative group of v_{O} out of the all $V_{a,p,d(1,2)}$ possibilities.

Our MC simulation works by extracting oxygen ions from the lattice similar to how a Galton-board arranges balls [58], where the resulting balls-filled columns' heights would represent the different v_{O} -configurational probabilities for a certain number of vacancies arranged in the octahedra. As such, for a given adiabatic temperature and a number of v_{O} , up to 1×10^5 MC trials are performed, including sets of trials for several MC random seeds, and the frequency of occurrence of a particular configuration characterized by a specific group of locations for the vacancies and with a specific local magnetic ordering is translated to the probability P_k , which is normalized over all the possible arrange-

ments such that $\sum_k P_k = 1$. The average magnetization $\langle M \rangle_k$ of each configuration k is addressed by using the Fe magnetic moments predicted by the hybrid-DFT model for each $V_{a,p,d(1,2)}$ type within the arrangement. The final magnetization for the deficient perovskite, for a given oxygen deficiency, is then calculated as:

$$\langle M \rangle = \sum_k P_k \langle M \rangle_k \quad (1)$$

Equation 1 uses a distribution that is obtained by sampling according to a stationary Markov process, i.e., the occurrence of a configuration with a certain number of vacancies depends on the probability of occurrence of a particular configuration with one less vacancy.

On the other hand, magnetic orderings used in the MC simulations are bound to the spin-polarization and supercell v_{O} -density modeled through DFT here, which in this case means scenarios where magnetism is dominated by the cations interaction in collinear solutions, one v_{O} /Fe-Fe pair approximately, as well as bath-temperatures for $k_b T$ below formation energies and spin-gaps (energy difference between FM to AFM local ordering). More aspects of our MC modeling are further discussed in next sections as well as in the appendices section. However, we will show next that these aforementioned approximations provide a powerful representation of one of the most important properties of a perovskite intrinsic magnet i.e., its spontaneous/saturation magnetization, and allows to understand better the role of the v_{O} -density in magnetic oxides synthesis.

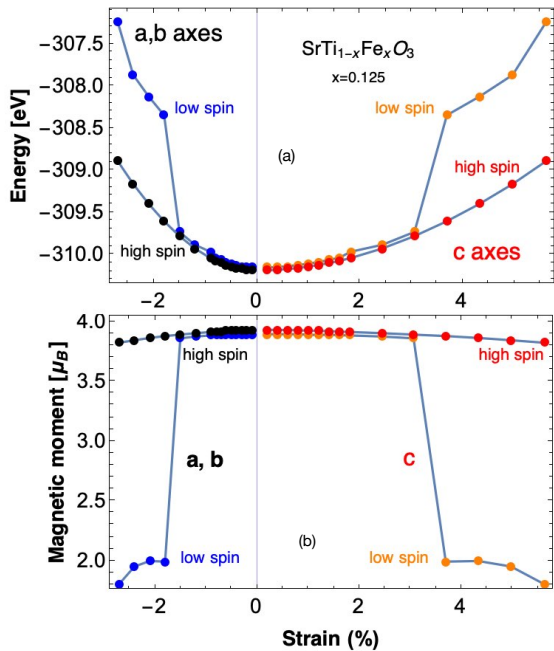


Figure 3: (a) Energy and (b) magnetic moment of STF with $x = 0.125$ and $\delta = 0$, for several tetragonal strains: in relaxations (GGA+U) Fe are initialized with Fe^{4+} low and high spin states. Black/blue curves correspond to the tetragonal (a, b) axes while red/orange correspond to the out-of-plane c axis.

Finally, we used the Interface Reaction of The Materials Project [59] to examine the magnetism of the compounds resulting in the reaction of two STO-based perovskites in contact [60]. The oxygen partial pressure and/or possible temperature effects are modeled by using a single chemical potential variable [59, 60]. The predictor provides us with the magnetic components' chemical fractions, which are then used to estimate the average magnetic moment [60] using the Materials Project database for the electronic properties of those components, and compare with our MC results and experiments.

3. DFT Results

3.1. Stoichiometric STF: $\text{SrTi}_{0.875}\text{Fe}_{0.125}\text{O}_3$

In “stoichiometric” STF ($\delta = 0$) the Fe ion would take a 4+ valence state to keep charge balance. This valence state is present e.g., in STF synthesized at high oxygen pressures > 1 atm [61]. Table 1 displays the energy characterization of STF as stabilized in high and low valence

Table 1: $\text{Sr}^{2+}\text{Ti}_{0.875}^{4+}\text{Fe}_{0.125}^{4+}\text{O}_3^{2-}$ (HSE06) lattice parameter, Fe magnetic moment and energies corresponding high/low spin initializations.

a' (Å)	S_i	μ_B/Fe	E_{S_i} (meV/f.u.)
7.81	h	3.73	$\mathbf{0.0}_{\text{gs}}$
7.79	l	1.98	68.2

spin-states for $x = 0.125$. It can be seen that the high spin in Fe corresponding to a (t_{2g}^3, e_g^1) 3d occupation is preferred over the low (t_{2g}^4, e_g^0) case. Metallic Fe/Co-based compounds are usually expected to be found in low spin states e.g., well known oxides such as magnetite Fe_3O_4 or SCO itself. However, in magnetite, Fe valence is strongly affected by electron exchange between the tetrahedral and octahedral sites increasing the Fe-spin to an intermediate value [62], while in the case of O-deficient SCO, an intermediate Co spin is favored by Co-Vacancy-Co coupling through the AFM shared electrons [31]. STF has a ~ 0.4 eV band-gap, as can be seen in Figure 2, which is bounded by the $\text{Fe}-e_g^1$ acceptor-like state, with such high spin preference is also deviating from the simplest molecular predictions.

This high spin seems robust with respect to tetragonal distortions, which are among the first factors lowering the crystal symmetry due to, e.g., substrate mismatch. As shown in Figure 3, large strains are needed to promote $10Dq$ changes. This last figure shows a high-to-low spin transition at $\sim 1.5\%$ in-plane strain. However, in order to capture such magnetic changes the relaxations have been constrained such that the perovskite single-crystal volume is averagely unchanged as it occurs, e.g., in STC where the substrate-mediated strain is balanced with chemical strain due to Co incorporation [47]. Full relaxed strain always leads to similar high-versus-low initialized magnetic results or elastically worse strain values. The ineffectiveness of these distortions are in accordance with Moreno et. al.[63], which suggested that metal-ligands distances are not so decisive in both the intrinsic e_g splitting and cubic field splitting $10Dq$. Bondings with deep 2s (free atom) orbitals, rather than shallow 2p ones, are essential to change orbitals occupations [33, 63].

Table 2: $\text{Sr}^{2+}\text{Ti}_{1-x}^{4+}\text{Fe}_x^{4+}\text{O}_3^{2-}$ properties for $x = 0.25$ (HSE06).

E_{S_i} (meV/f.u.) for configurations in Fig. 1 with S_i				
nn_{Fe_i}/a	$E_{h_{AFM}}$	$E_{h_{FM}}$	$E_{l_{AFM}}$	$E_{l_{FM}}$
1	32.5	0.0_a	33.6	201.0
$\sqrt{2}$	35.7_b	37.5	158.1	157.3
$\sqrt{3}$	37.2	36.4_c	36.3	167.6
Lattice parameters and magnetic structure for a, b, c				
$S_f^{1,2}$ (μ_B)	(a', b', c') (\AA)	V (\AA^3)	nn_{Fe_f}/a	E_{bg} (eV)
(3.7, 3.7) _a	(7.80, 7.80, 7.79)	474.66	~ 0.89	0.00
(3.7, -3.7) _b	(7.80, 7.80, 7.80)	474.70	$\sim 0.9\sqrt{2}$	0.01
(3.7, 3.7) _c	(7.80, 7.80, 7.80)	474.69	$\sim 0.9\sqrt{3}$	0.16

3.2. Stoichiometric STF: $\text{SrTi}_{0.75}\text{Fe}_{0.25}\text{O}_3$

We focus from this point onward on the composition corresponding to $x = 0.25$, which within our model perovskite means two Fe/u.c., as Figure 1 shows. These Fe cations can be arranged into three different distributions, which we considered and evaluated at high and low spin states for the corresponding valences and ferromagnetic/antiferromagnetic local spin orderings. In Table 2 hybrid relaxation results are presented, where $E_{(h,l)_{FM,AFM}}$ describes the energy difference of the specific state with respect to the global ground state among all. $nn_{\text{Fe}_{i,f}}/a$ and $S_{i,f}$ are the proper initial and final Fe-Fe supercell distances and local magnetic moment, respectively. We select for each Fe distribution the lowest energy state being the global ground state corresponding to the ferromagnetic $E_{h_{FM}}$ high-spins ordering. The first two major suggestions of Table 2, which already differ qualitatively from what happens for instance in STC [31] are: the magnetic cations stabilized preferably at a first nn_{Fe} configuration respect to the B-B (ABO_3) possibilities, Figure 1(a); high spin states dominate the stabilized magnetism, which follows previous section' conclusions.

In Table 2 the energies of the low spin states that are comparable to those of high spin states are due to self-consistent switching to high spins. Further constrictions to force those low states lead to higher energies as already shown by Figure 3 and other results in Table 2, with energies over ~ 150 meV in this last case. Comparatively, the intermediate distance between the Fe ions is the one allowing an AFM ordering, while in STC it stabilizes the ground state in a FM configuration.

In this $\delta = 0$ case, for the systems it is energetically less expensive to arrange an AFM ordering by switching one of the two spins than stabilizing larger nn_{Fe} . It is observed that the $E_{h_{AFM}}$ energy increases as nn_{Fe}/a increases while keeping AFM local moments, however, if the local moments are kept FM the system seems to experience a disconnection when Fe ions are pulled apart. They stabilize the same in whatever location they are placed in, not without a huge energetic cost from the ground state. The results in Table 2 therefore witness the different exchange-coupling nature that links the Fe ions in these three configurations i.e., the oxygen mediates magnetic interactions through super-exchange mechanisms that in this Fe-substituting case seem negligible beyond B-B first nearest-neighbors.

Our stoichiometric STF in Table 2 is then suggesting that if a real sample were not to be monocrystalline but is conformed by at least a couple of domains due to effects such as e.g. strain, chemical pressure, annealing, or cations/anions defects, a mixture of FM and AFM local orderings would be stabilized giving rise to an average magnetization observable independent of the resulting magnetic ions sub-lattice. However, the energy weight of a $[1, 0, 0]$ Fe-cations crystalline symmetry and the magnetic switching of this last one would be statistically preponderant among other configurations.

3.3. Oxygen deficient STF: $\text{SrTi}_{0.75}\text{Fe}_{0.25}\text{O}_{2.875}$

For STF, the magnetization as a function of the oxygen pressure during growth was depicted in References [10, 30], and it was clear that there is a tuning process that is triggered by the oxygen

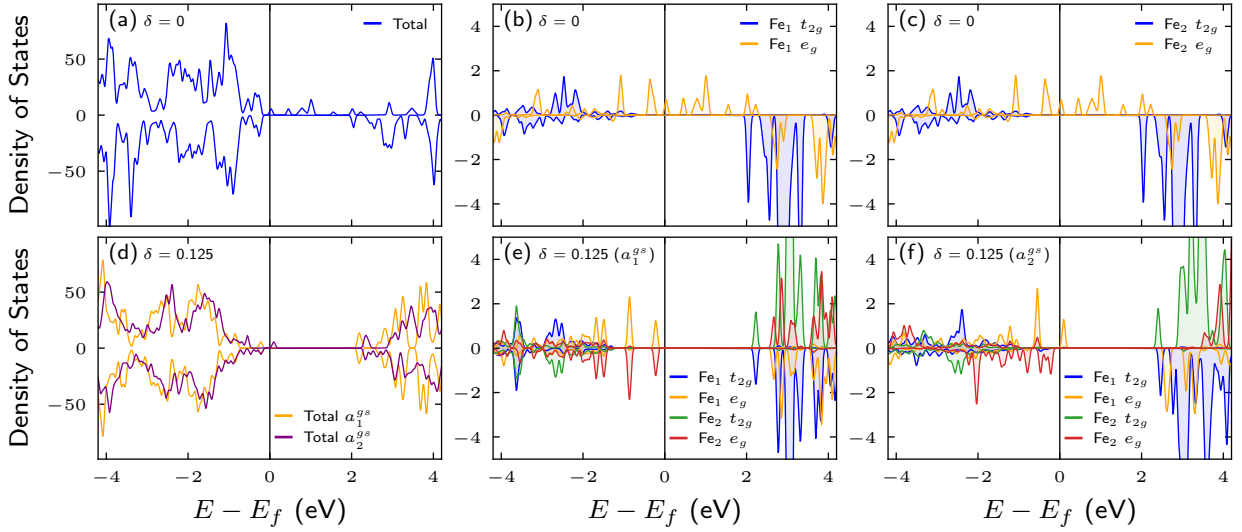


Figure 4: (a) Total DOS and (b, c) $t_{2g}e_g$ -projected DOS of Fe₁ and Fe₂ for the ground state stoichiometric STF. (d) Total DOS and (e, f) $t_{2g}e_g$ -projected DOS of Fe ions for the $V_{a_{1,2}}$ vacancies ground states in SrTi_{0.75}Fe_{0.25}O_{2.875}.

vacancies, in which a maximum is reached at some v_o density and then a demagnetization-like process is observed. In this final DFT section, we analyze the magnetic behavior of STF for $x = 0.25$ and $\delta = 0.125$ i.e., one vacancy/supercell. As we will show in what follows, this is enough to give a step forward in understanding the experimental behavior and to set the bases for more complex or computationally demanding descriptions.

Figure 1 shows the five different vacancies that are found to be symmetrically irreducible for all the Fe-Fe cations configurations, according to our considerations in Section 2. In Table A.4 we summarized all the results for $nn_{\text{Fe}_i}/a \sim 1$, in which FM and AFM states have been relaxed for the corresponding valences of a neutral formula. The sub-indices a_1 or a_2 label the vacancies according to Figure 1. We can see that both a_1 and a_2 gs are given by AFM states with what seem to be high Fe spins. Those two systems, though they have the vacancies coordinating a Fe ion, both present different resulting structures i.e., a tetragonal and an orthorhombic-like, respectively, which means that the Fe- v_o -Fe configuration reduces less the symmetry of the system, what prompts it to be the global ground state among competing a_1^{gs} and a_2^{gs} as Table A.4 shows. This is also reflected in the magnetic moments, where we see in a_2^{gs} two slightly unequal moments differing by $\sim 0.1\mu_B$,

which is a consequence of the different hybridized $3d$ -Fe occupations displayed in Figure 4. This last figure shows the total and $t_{2g}e_g$ densities of states for the gs in the stoichiometric and $a_{1,2}$ deficient cases. For $\delta = 0$, the system is FM and both spins are in similar states with polarized seemingly half-filled $t_{2g}e_g$, which would correspond to a $t_{2g}^3e_g^1$ occupancy for Fe_h⁴⁺ spin states. In a_1^{gs} , Fe cations are AFM ordered and in similar states, i.e., an occupancy close to a $t_{2g}^4e_g^2$ for Fe_h²⁺ spin states. When checking a_2^{gs} in Figure 4, we found the solution associated to the mixture of valences spin states, for an AFM ordering, which agrees with the reported ferrimagnetic-like behavior found in STF [10]: the Fe ion that lies on the incomplete O₅ octahedra, here called Fe₂, seems to have an electronic distribution of a hybridized $t_{2g}^3e_g^2$ for a Fe_h³⁺ character and therefore larger local magnetic moment than Fe₁, which resembles the Fe state in the previous cases.

One deficient solution for V_{a_1} provides us with local annihilation of the magnetization, while a second one V_{a_2} , provides us with a small magnetization. One can already intuit that one way of increasing or decreasing the perovskite magnetization is to let the system stabilize not just one type of v_o , which is less plausible experimentally either way, but a group of solutions within a reasonable energy formation. These two vacancies $V_{a_{1,2}}$

happen to have spin-gaps, for FM states to/from AFM ones, just below a few dozen meV, which one could imagine competing with a room temperature excitation threshold for thermal activation up to some extent.

We now describe briefly the rest of the v_o considered here. Tables A.5 and A.6 present the characterization of the $[1, 1, 0]$ (plane) and $[1, 1, 1]$ (diagonal) arrangements, respectively. The first one displays the results corresponding to V_{p_1} and V_{p_2} in Figure 1. In this cations distribution the AFM and FM stabilized solutions are energetically close, as the gs for $V_{p_{1,2}}$, both AFM, are within just a couple of meV off the closest FM state, which also present high spin occupation. In both cases, the vacancy coordinates one Fe ion, and therefore one of the Fe magnetic moments is always larger than the other one, in a similar manner to the behavior of Co observed in STC [31]. In this last case, though, the difference is due to a low-to-high spin state transition, while in STF it originates from hybridization between high Fe^{4+} and Fe^{3+} states as Figure 5 suggests. Hence, the system relaxes to a magnetized state, either conformed by a ferrimagnetic ordering with $\sim 0.05\mu_B/Fe$ or by a FM one with $\sim 4.16\mu_B/Fe$, respectively. The energy difference between these orderings seems independent of the V_p type as well as the local Fe magnetic moments.

Although here we are interested in the magnetic degrees of freedom and V_{p_1} and V_{p_2} behave similarly from that viewpoint, among those two v_o the first one turns out to be more interesting for multiferroic purposes as the $3d$ hybridization is slightly shifted just below E_f and the system is a semiconductor with a 2.15 eV band-gap, which is adequate for searching of an effective electric polarization in non-metallic ferroelectrics, as it was explored in STFC [34]. In this last work, the authors showed how oxygen migrations and deficiency variations can modulate the band-gap and electric polarization in Fe, Co-substituted STO systems with defects such as the ones studied here.

Figure 5 shows the total and projected density of states for V_{p_1} . It is clear that the system is AFM and that different $3d$ -occupancy determines the magnetism of the solid solution, in spite of the close local spin values. One spin is stabilized

in a $t_{2g}^3e_g^1$ while the other one in a $t_{2g}^4e_g^2$. The subtle but consistent up-down population in one of the two t_{2g} orbitals (Fe_2) of the ground states in Table A.5, which is also present in several of the less stable ground states, differentiates the two magnetic states of the Fe ions sufficiently as to have an effective magnetic moment/supercell in what is the aforementioned ferrimagnetic ordering.

We now analyze V_{d_1} in Figure 1. Table A.6 shows that in this configuration the system stabilizes an AFM ordering. A FM solution ($d_1^{ss_1}$) is within a very narrow energy difference, which is a repercussion of the large $nn_{Fe_i}/a \sim \sqrt{3}$ distance compared to an O-mediated nn_{Fe} super-exchange. Isolate-like Fe ions are coordinated by completed octahedra in two crystallographic directions but $[100]$, creating a tetragonal-pyramid chemical strain that slightly favors indirect antiferromagnetism, in accordance with a quasi-static d^4-d^6 180° bond after Goodenough [29]. The second lowest energy state is also AFM though it is not equivalent to d_1^{gs} . The slightly compact packaging of ss_1 promoted a shifting of the e_g in Figure 5 which creates available hybridized states that prevent the energy band-gap. The magnetic moments are given by high spin states following the behavior exhibited by $V_{p_{1,2}}$, which stabilized $t_{2g}^3e_g^1$ and $t_{2g}^4e_g^2$ spin states, with the vacancy surrounding the first one (Fe_1). Also, d_1^{gs} has a band-gap of 2.04 eV, which is larger than the one for the V_p case but not necessarily larger than the one for V_{a_1} . This indicates that ions-proximity is not a predominant factor in the metallic-like effects due to cluster formation in perovskite solid solutions of this kind when we consider v_o . For instance, in semi-metallic SCO a gap opens up and increases with δ while perovskites such as Fe, Co-substituted STO present a maximum at intermediate vacancy density [34] for different cations nn distances.

4. MC Results

We are interested in implementing a model that could give us further insights to understand the change of magnetization when the number of vacancies increases. In this section, we display the results of the Monte Carlo approach described in Section 2. Such a model is able to capture some characteristics of the deficient perovskite magnetism when its magnetic remanence and saturation magnetization are similar, which can be reached by using different substrates and/or

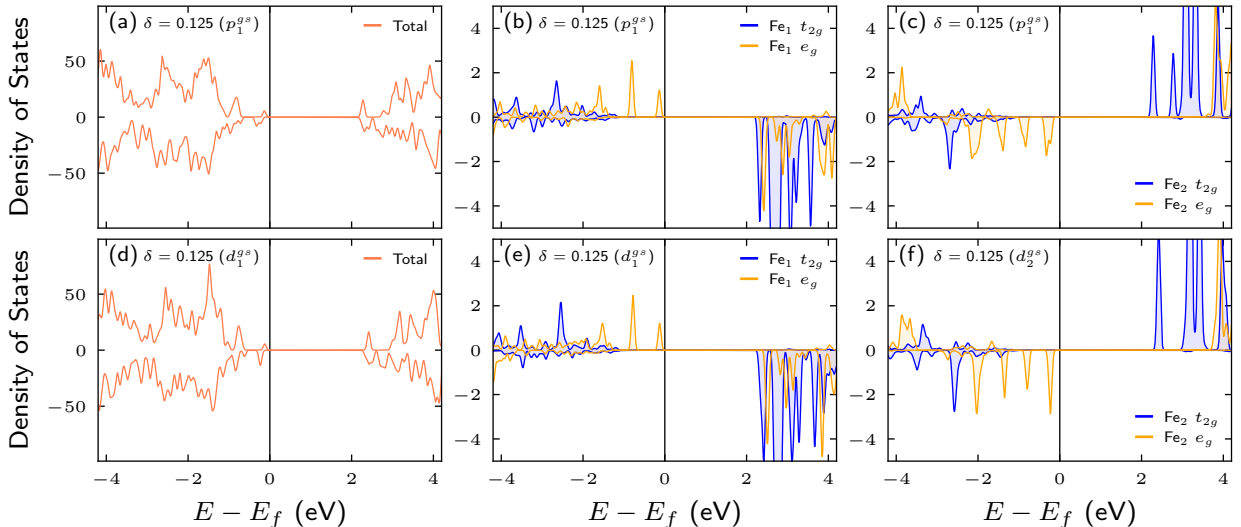


Figure 5: (a) Total DOS and (b, c) $t_{2g}e_g$ -projected DOS of Fe ions for the V_{p_1} vacancy ground state in $\text{SrTi}_{0.75}\text{Fe}_{0.25}\text{O}_{2.875}$. (d) Total DOS and (e, f) $t_{2g}e_g$ -projected DOS of Fe ions for the V_{d_1} vacancy ground state in $\text{SrTi}_{0.75}\text{Fe}_{0.25}\text{O}_{2.875}$.

tuning the deposition pressures [10, 30], in hard and soft magnetic materials [29].

Among all the v_o results in Tables A.4, A.5 and A.6, we selected a group of vacancies that represent an STF solution with the same magnetic cations arrangement. The supercells in Figure 1 give rise to STF crystals with just one of three Fe-Fe arrangements each; therefore, if the ab-initio energies are approached as statistical weights, those would meaningfully represent a monocrystal i.e., there is no mixture of $[1, 0, 0]$, $[1, 1, 0]$ and/or $[1, 1, 1]$ arranged Fe-Fe magnetic pairs in our scope. Now, to check which vacancies are energetically favorable in each configuration, we calculate the formation energy E_f^δ for the gs and ss of each $V_{a,p,d}$. In Table 3 we can see the formation energy E_f^δ of oxygen vacancies as calculated with Equation 2:

$$E_f^\delta = E_\delta - E_{\delta=0} + \mu_{\text{O}} \quad (2)$$

where E_δ is the total energy of the crystal with one oxygen vacancy after relaxation, and $E_{\delta=0}$ is the total energy of the stoichiometric crystal ($\delta = 0$) with the corresponding Fe-Fe pair orientation. μ_{O} is the chemical potential of O, calculated as half the energy of an isolated O_2 molecule [65].

In the case of V_{d_1} we have used ss_2 , as ss_1 and gs converged to the same magnetically, and because ss_2 is FM as opposed to gs , which happens with the gs and ss for $V_{a,p}$ too. Table 3 confirms that

Table 3: v_o formation energies E_f^δ and space group (SG) symmetry for gs/ss in Tables A.4, A.5 and A.6 (HSE06).

E_f^δ (eV)	V_{a_1}	V_{a_2}	V_{p_1}	V_{p_2}	V_{d_1}
gs	3.74	4.21	3.94	3.90	3.92
ss	3.98	4.40	3.95	3.91	3.92
SG	P4/mmm	Pmm2	P4mm	Pmm2	P4mm

the diagonal configuration places the Fe ions too far for them to sense the switching of the magnetic coupling and/or slight tetragonal distortions; therefore, we have practically energy-equivalent vacancies for this configuration. Creating these last v_o is cheaper than creating V_{p_1} but slightly more expensive than V_{p_2} , which is a consequence of the in-plane structural changes due to the $[1, 1, 0]$ Fe-ions arrangement that are evenly competing with the Ti- v_o -Fe chemical strain caused by V_{p_2} [31], as symmetry in Table 3 evidences. Among all v_o in Table 3 V_{a_1} is energetically cheaper to create although V_{a_2} is comparably more expensive. Nevertheless, the $[1, 0, 0]$ Fe-Fe $\delta = 0$ configurations are cheaper overall when revisiting Table 2. Moreover, V_{a_1} and V_{a_2} can be connected by adiabatic oxygen migration paths that support ferroic orders [34], besides that there is a difference between the in-plane and the out-of-plane experimental magnetization in STF, which is related to the influence of magnetoelastic

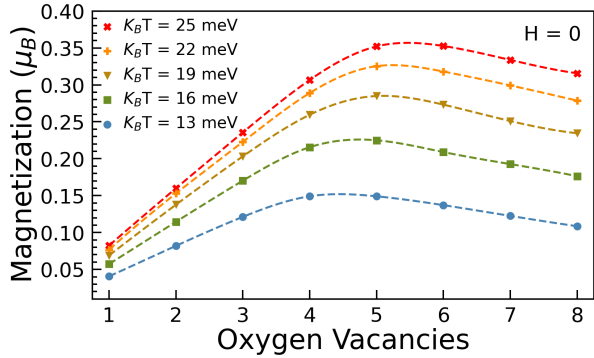


Figure 6: DFT based Monte Carlo modeling of oxygen deficient STF ($x = 0.25$) magnetization for different number of v_o . Figure B.10 displays the MC scheme implemented to get these magnetizations.

effects that could promote the formation of vertical nanopillars within the perovskite matrix, orienting the resulting magnetization [10]. These previous observations leave us with the choice of the “above” configuration as well as with the energy results in Table A.4 as a reasonable representative STF configurational space to be sampled by our Monte Carlo modeling.

We then created vacancies in a $[1, 0, 0]$ Fe-Fe oriented MC model-crystal starting from a stoichiometric solution. While increasing the number of vacancies such that δ ranges from 0.0 to 0.125, this last value being among the intermediate values at which the ferroic order parameters have been suggested to be maximized for $\text{SrTi}_{1-x}\text{Fe}_x\text{O}_3$ with $x = 0.25$ [31, 33, 34], we apply two constrains: (i) v_o can take either a V_{a_1} or a V_{a_2} character/location by bearing the gs/ss corresponding energies, associated Fe magnetic moments and corresponding Fe-Fe alignments predicted by our DFT models; (ii) interactions between “above” Fe-Fe aligned pairs of magnetic cations, separated at least by $2a'$, are negligible. Vacancy interactions in this $\text{ABO}_{3-\delta}$ solid solutions as well as charging effects due to these defects are also likely to be negligible as suggested by this and other ab-initio modelling [33]. Finally, we run Monte Carlo simulations by “throwing” vacancies to the O-octahedral sublattices while following the algorithm illustrated in Figure B.10 and the description in Section 2. From the stochastic method, frequencies of specific vacancies-configuration occurrence are obtained, which are then translated to normalized probabilities to be used in Equation 1.

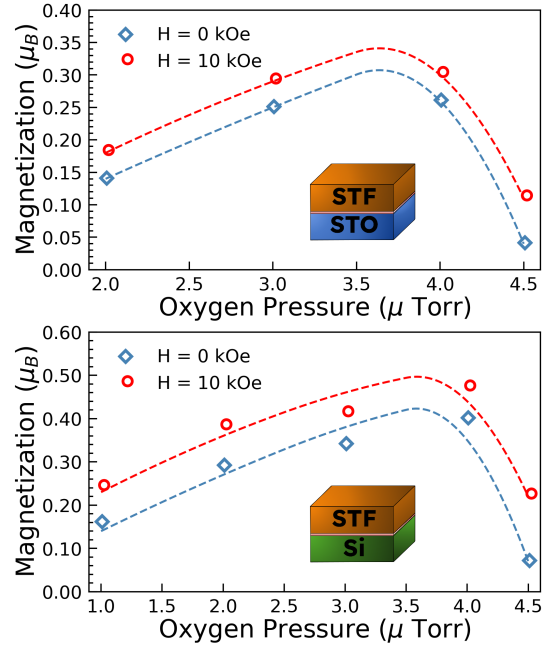


Figure 7: Experimental out-of-plane magnetization for oxygen deficient STF films deposited on (a) STO; (b) Si. Selected data reproduced from Ross et al. [10] for remanence and saturation magnetizations. Dashed lines are interpolating guiding lines.

Figure 6 displays the modeled magnetization results in the absence of a magnetic field for oxygen deficient STF. For all the adiabatic bath-temperatures simulated here the magnetization has a similar behavior i.e., it increases linearly from low values $\sim 0.05 - 0.1\mu_B$, to then smoothly reaching a maximum of $\sim 0.35\mu_B$ at intermediate oxygen deficiency $\sim \delta = 0.093$ ($\sim 6 v_o$); then, if the number-of-vacancies/deficiency keeps increasing, such magnetization slowly decreases but with a lesser linear slope than the one it followed to reach its maximum. To compare our intuitive model with experiments, we have extracted from the STF hysteresis loops at room temperature reported in Ross et al. [10] the data representing the remanence ($H=0$ kOe) and saturation magnetization ($H=10$ kOe). Figure 7 displays such magnetizations taken at different values of oxygen pressure during deposition.

Figure 7 shows STF magnetization features already remarkably predicted by Figure 6. Aforementioned behavior of the magnetization in the model figure is also present in the experimental

results. In fact, although the relation between the number/density of vacancies and the oxygen pressure during deposition in these kind of experiments is still an open question and several models have been proposed [34, 61], what is clear is that high oxygen pressures mean a lower content of oxygen vacancies and low pressures give rise to large content of v_o . Therefore, Figures 6 and Figure 7 should be read such that the linear behavior below $\sim 5 - 6 v_o$ in the modeling results, which have a faster slope, correspond to the linear behavior for high pressure in the experimental results, which also is the linear part with the faster slope. Slowly decreasing of the magnetization in the modeling when there are more vacancies also represent well the slower decreasing of the magnetization in the experiments, and the threshold given by the saturation magnetization at room temperature (~ 25 meV) is also captured.

If a logarithmic model is used to read the oxygen deficiency δ out of the oxygen pressure [61], and it is applied to relate Figure 6 and Figures 7, our model would differ from the experimental results in terms of the location of the maximum of the magnetization by an oxygen deficiency that would be equivalent to a couple of v_o i.e., in Figures 7 the decreasing of the magnetization happens at higher oxygen pressures. One possible reason for this is that the experimental results are performed for a slightly higher Fe content, 0.8 Fe ions/supercell more for $x = 0.35$ compared to our stoichiometry, which for an oxygen content given by $3 - x/2 + \delta'$ in Tuller's model [61] means less deficiency δ for $x = 0.35$ in our case, and therefore higher oxygen pressures. Aforementioned model for the oxygen content in STF has been applied at higher temperatures too, nevertheless, Figures 7 were obtained at room temperature, so to read the relation between oxygen pressure and number of v_o with such model-curves would inherently include a temperature shifting effect, which is originated on the increasing of oxygen content for a given pressure when the temperature decreases. In Figure 6 we showed that the location of the representative maximum of magnetization can be shifted when the temperature is changed. For a given number of vacancies the magnetization decreases if the temperature decreases.

The ability of our MC simulations to reproduce these previous characteristics is based on the fact

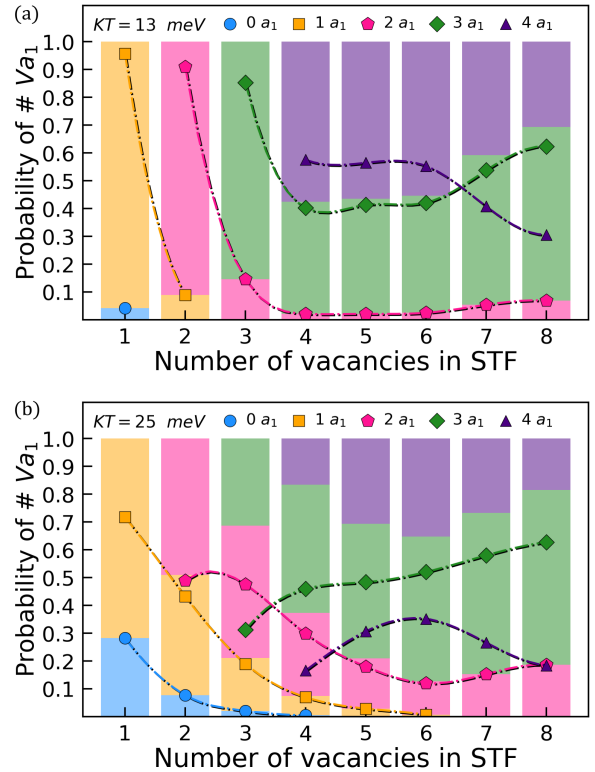


Figure 8: Probability of occurrence of specific types of vacancies among V_{a_1} and V_{a_2} for a given δ and a bath temperature corresponding to KT e.g., 13 meV (a), and 25 meV (b). For the sake of simplicity, as $P(l)_{V_{a_1}} + P(n)_{V_{a_2}} = 1$, it is normalized for $(l+n) = \#$ of $v_o \implies \delta$, we plot just $P(l)_{V_{a_1}}$ such that the probability $P(l)_{V_{a_1}} \longrightarrow$ (symbol) l_{a_1} . We have alternatively used in the background %-bars of the same markers' colors to illustrate the quantity of l_{a_1} that would results out of the total number trials in the MC simulations.

that a great portion of the effects observed in Figures 7 is due to bulk-like magnetic orderings that are thermally activated. In Figure 8 we have displayed the distribution of the probabilities for the occurrence of a specific number of $V_{a_{1,2}}$ when the temperature is modified. These last figures show that while for low temperatures is less likely to have V_{a_2} , for room-temperature such probability has increased and therefore the one of having a nonzero magnetization as the V_{a_2} has finite magnetization for either FM and AFM polarization; FM ordering increases faster the magnetization though, however, it comes with higher energetic price. When the number of vacancies increases the probability of having less V_{a_1} and more V_{a_2} increases for a given temperature, this is also because of a topological factor that is rather

difficult to measure microscopically i.e., there are more Ti- V_{a_2} -Fe possible sites than Fe- V_{a_1} -Fe ones. So, as the bars in Figure 8 suggests, when there are more possible vacancy sites than actual vacancies and the temperature is low the magnetization increases until a quasi-even distribution between $a_{1,2}$ *gs*. Once the number of vacancies competes with the available sites the contribution from a_1 does not increase anymore while a_2 does with mainly antiferromagnetic contributions that are now decreasing the magnetization. This last of course happens slower than the magnetization process with few vacancies that was dominated by FM contributions. If the temperature increases, it promotes the apparition of new V_{a_2} rather than *gs* to *ss* transitions in V_a as lower panel in Figure 8 shows, and the magnetization for a sufficient number of vacancies will slowly start to decrease more due to a AFM versus FM competence within V_{a_2} -given orderings than to the competence between the different types of v_o .

Finally, the beautiful balanced competence between what we could call “Fe-Fe magnetic defects” that we just described is a bulk-like magnetism that dominates the magnetic ordering in these systems. Nonetheless, there is another factor that contributes nicely to the “quenching” shaping of the magnetization that we observed in Ross’s et al. results [10] i.e., the magnetism that emerges at the interface between the bulk perovskite and the substrate. Although a deeper study of this part of the system is beyond our scope here, we have asked ourselves what would be the behavior of the magnetic moments at that interface; if in fact it is small compared to the bulk-film, its contribution to the changes of the magnetization samples would come mainly from the changes that experience the local magnetic moments themselves when the oxygen content is changed and therefore different oxides, among stabilized low/high members of the STF family, contribute with different Fe-stabilized magnetic moments. In Figure 9 we display the results for the averaged magnetic moments at the interface obtained as described in our Section 2, by applying the Materials Project’ Interface Reaction [54, 59, 60]. In this case we simulate STF/STO interface for three different initial interface compositions and 50% Fe substitution value. This last value was the substitution with more data available at the Materials Project’ database for this interface. Figure 9 shows that the interface mate-

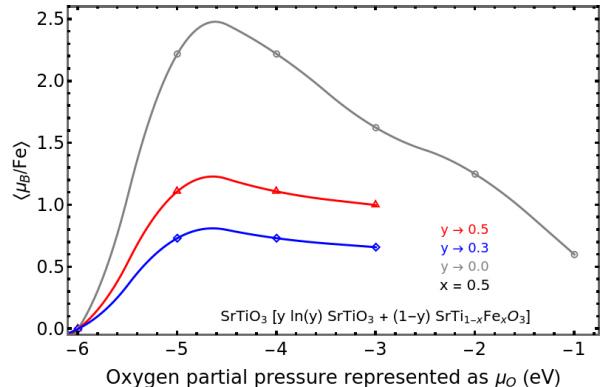


Figure 9: Magnetism at STO/STF interface versus the oxygen-gas chemical potential μ_O . Simulations of the averaged Fe magnetic moment at the resulting interface solution obtained by applying the Interface Reaction of the Materials Project [54, 59, 60]. Solid colored lines are guiding lines.

rial is able to stabilize low spin states, with intermediate values for the oxygen-gas chemical potential being able to mix what could be 3+ and 2+ Fe low spins for lower STF content. By increasing Fe content through STF, the system begins to recover the bulk-film behavior, with 4+ low occupancy being favored. Therefore, the interface also contributes to the “quenching” shaping of the magnetization by tuning the Fe moments among low spin states, which range within $(0 - 2)\mu_B$. In fact, it is possible to find for large chemical potentials interface-compounds with magnetic contributions arising from Ti ions, which would be in accordance with recent studies in oxygen deficient STO and STFC [34] that found magnetic Ti sub-lattices in the perovskite matrices.

5. Conclusions

We have performed Hybrid-DFT calculations, Monte Carlo simulations as well as reaction-data’ magnetic interpretation to model the saturation/remanence magnetization in oxygen deficient STF. We have shown that the experimental behavior is likely due to three main factors: (i) competition between specific “magnetic defects” conformed by Fe cations that are coordinated by energetically different v_o , which gives rise to different local spins and magnetic alignments. (ii) The Fe cations distribution in relation to the density of v_o plays an important role in defining the oxygen pressure at which the magnetization

increasing-process triggered by the AFM to FM local switching starts to be reverted by thermally activated topologically-different “magnetic defects”, which end up giving to the material a ferrimagnetic character. (iii) The magnetic cations at the interface can present a variety of low spin states, in contrast to the high-spin dominated occupancy in the bulk-film material, which on average decreases the magnetic moment per Fe for larger and very low oxygen partial pressures.

A full magnetic simulation of this experimental situation would require a many-body Hamiltonian + ab-initio/Molecular dynamics modeling at finite temperature, in which overwhelming simulations for different number of ions would require the microscopic parameters to be calculated self-consistently. It would also require very large supercells if we were to consider all the different configurations for the magnetic ions and vacancies in the structural relaxations at once, which in turn would multiply the configurational space several times as well as the negative magnetic solutions. That would be computationally prohibitive even for some non hybrid functionals. Faster semi-local/meta functionals would require us to constrain the systems to some stabilized valence spin states [76], while lacking the compromise between magnetic and conductive properties of hybrids [33]. Our approach on the other hand, is able to capture useful characteristics that can be used as fingerprints to synthesize new materials and train Machine Learning based simulations at an affordable computational cost.

For a magnet its value of saturation is determinant in terms of e.g., knowing how much magnetic field we need to switch it, as well as its remanence is a witness of the hysteresis process. Our model does not capture hysteresis features, however, we are mostly looking for square-like type of magnets that could be useful for storage/processing information, permanent magnets, energetically efficient switchable systems or with multiferroic features. The model presented here is robust with respect to the representation of the polarized states of a material degrees of freedom that give rise to most characteristics of those aforementioned types of magnets. Moreover, this investigation provides us with hints about the type of crystal symmetry that should be targeted. Thinking in a specific saturation magnetization to be reached for

a particular deficiency or working temperature, or vice versa, we could improve on using δ so we can tailor the magnets saturation features by making use of the properties described here.

6. Acknowledgements

J.M. Florez and E.S. Morell thank support from project FONDECYT Regular 1221301, Agencia Nacional de Investigación y Desarrollo (ANID), Chile. M.A. Solis thanks financial support of USM-DPP, Chile. C.A. Ross thanks National Science Foundation: DMR 1419807.

J.M. Florez also thanks Prof. Shyue P. Ong from the Department of NanoEngineering at the University of California, San Diego, for helpful discussions about the Materials Project’ tools for oxygen deficient perovskites modeling.

Appendices

Appendix A. STF for $\delta = 0.125$ and $x = 0.25$

Table A.4: $\text{Sr}^{2+}\text{Ti}_{0.75}^{4+}\text{Fe}_{0.25}^y\text{O}_{2.875}^{2-}$ properties for vacancies $\mathbf{V}_{\mathbf{a}_1}$ and $\mathbf{V}_{\mathbf{a}_2}$ (HSE06). FM and AFM energies of $nn_{\text{Fe}} \sim a'$ configurations for each initial $S_i^{1,2}$ Fe spins, as well as lattice parameters, magnetic structure, band-gap and relative energy of the selected gs and ss states.

y	$S_i^{1,2}$	$\mathbf{V}_{\mathbf{a}_1}$		$\mathbf{V}_{\mathbf{a}_2}$	
		E_{FM} (meV/f.u.)	E_{AFM} (meV/f.u.)	E_{FM} (meV/f.u.)	E_{AFM} (meV/f.u.)
(2+,4+)	h, h	248.3	$-_{gs}$	98.9	0.02
	h, l	222.5	107.9	223.7	134.9
	l, h	236.1	233.7	206.6	197.6
	l, l	108.3	108.4	78.8	135.3
(4+,2+)	h, l	238.1	232.8	197.6	197.5
	l, h	222.8	107.9	234.8	135.6
	l, l	107.9	108.0	135.2	135.2
(3+,3+)	h, h	31.2 $_{ss}$	0.06	23.8 $_{ss}$	$-_{gs}$
	h, l	313.3	234.8	268.6	197.4
	l, h	313.3	233.3	196.9	197.6
	l, l	447.9	218.2	408.3	0.02
State	$S_f^{1,2}(\mu_B)$	(a', b', c') (\AA)	V (\AA^3)	E_{bg} (eV)	$\Delta E_{a_1^{gs}}$ (meV/f.u.)
a_1^{gs}	(4.07, -4.07)	(7.82, 7.82, 7.83)	479.33	2.15	—
a_1^{ss}	(4.14, 4.14)	(7.82, 7.82, 7.84)	479.65	0	31.2
a_2^{gs}	(4.07, -4.17)	(7.83, 7.85, 7.83)	481.48	0	59.6
a_2^{ss}	(4.14, 4.22)	(7.84, 7.84, 7.84)	481.72	0	83.4

Table A.5: $\text{Sr}^{2+}\text{Ti}_0.75^{4+}\text{Fe}_{0.25}^y\text{O}_{2.875}^{2-}$ properties for vacancies $\mathbf{V}_{\mathbf{p}_1}$ and $\mathbf{V}_{\mathbf{p}_2}$ (HSE06). FM and AFM energies of $nm_{\text{Fe}} \sim a'\sqrt{2}$ configurations for each initial $S_i^{1,2}$ Fe spins, as well as lattice parameters, magnetic structure, band-gap and relative energy of the selected gs and ss states.

y	$S_i^{1,2}$	$\mathbf{V}_{\mathbf{p}_1}$		$\mathbf{V}_{\mathbf{p}_2}$	
		E_{FM} (meV/f.u.)	E_{AFM} (meV/f.u.)	E_{FM} (meV/f.u.)	E_{AFM} (meV/f.u.)
(2+,4+)	h, h	112.4	0.001	94.0	0.001
	h, l	166.1	128.9	275.0	143.4
	l, h	230.9	165.6	210.7	193.2
	l, l	371.7	129.3	93.0	143.4
(4+,2+)	h, l	165.5	165.6	193.6	193.4
	l, h	217.4	129.2	319.8	142.0
	l, l	143.5	129.5	143.4	143.4
(3+,3+)	h, h	0.8 _{ss}	0.002	0.6 _{ss}	0.008
	h, l	166.1	165.6	273.7	194.0
	l, h	209.4	165.6	223.7	193.2
	l, l	371.8	— _{gs}	400.4	— _{gs}
State	$S_f^{1,2}(\mu_B)$	(a', b', c') (Å)	V (Å ³)	E_{bg} (eV)	$\Delta E_{p_2^{gs}}$ (meV)
p_1^{gs}	(4.12, -4.19)	(7.83, 7.83, 7.86)	481.38	1.94	5.1
p_1^{us}	(4.12, 4.19)	(7.83, 7.83, 7.85)	481.51	0	5.9
p_2^{gs}	(4.12, -4.20)	(7.84, 7.85, 7.83)	481.57	0	—
p_2^{us}	(4.12, 4.20)	(7.84, 7.84, 7.83)	481.25	0	0.6

Table A.6: $\text{Sr}^{2+}\text{Ti}_0.75^{4+}\text{Fe}_{0.25}^y\text{O}_{2.875}^{2-}$ properties for vacancy $\mathbf{V}_{\mathbf{d}_1}$ (HSE06). FM and AFM energies of $nm_{\text{Fe}} \sim a'\sqrt{3}$ configurations for each initial $S_i^{1,2}$ Fe spins, as well as lattice parameters, magnetic structure, band-gap and relative energy of the selected gs and ss states.

y	$S_i^{1,2}$	E_{FM}	E_{AFM}	
		(meV/f.u.)	(meV/f.u.)	
(2+,4+)	h, h	105.1	— _{gs}	
	h, l	306.9	132.4	
	l, h	215.5	172.5	
	l, l	102.9	132.7	
(4+,2+)	h, l	273.3	172.3	
	l, h	231.0	132.9	
	l, l	144.0	132.4	
(3+,3+)	h, h	0.04 _{ss2}	0.1	
	h, l	174.2	172.3	
	l, h	215.2	172.3	
	l, l	382.9	0.1 _{ss1}	
State	$S_f^{1,2}(\mu_B)$	(a', b', c') (Å)	V (Å ³)	E_{bg} (eV)
d_1^{gs}	(4.12, -4.12)	(7.83, 7.83, 7.85)	481.83	2.04
d_1^{ss1}	(4.12, -4.12)	(7.83, 7.83, 7.85)	481.51	0
d_1^{ss2}	(4.12, 4.12)	(7.83, 7.83, 7.85)	481.62	0

Appendix B. Monte Carlo modeling

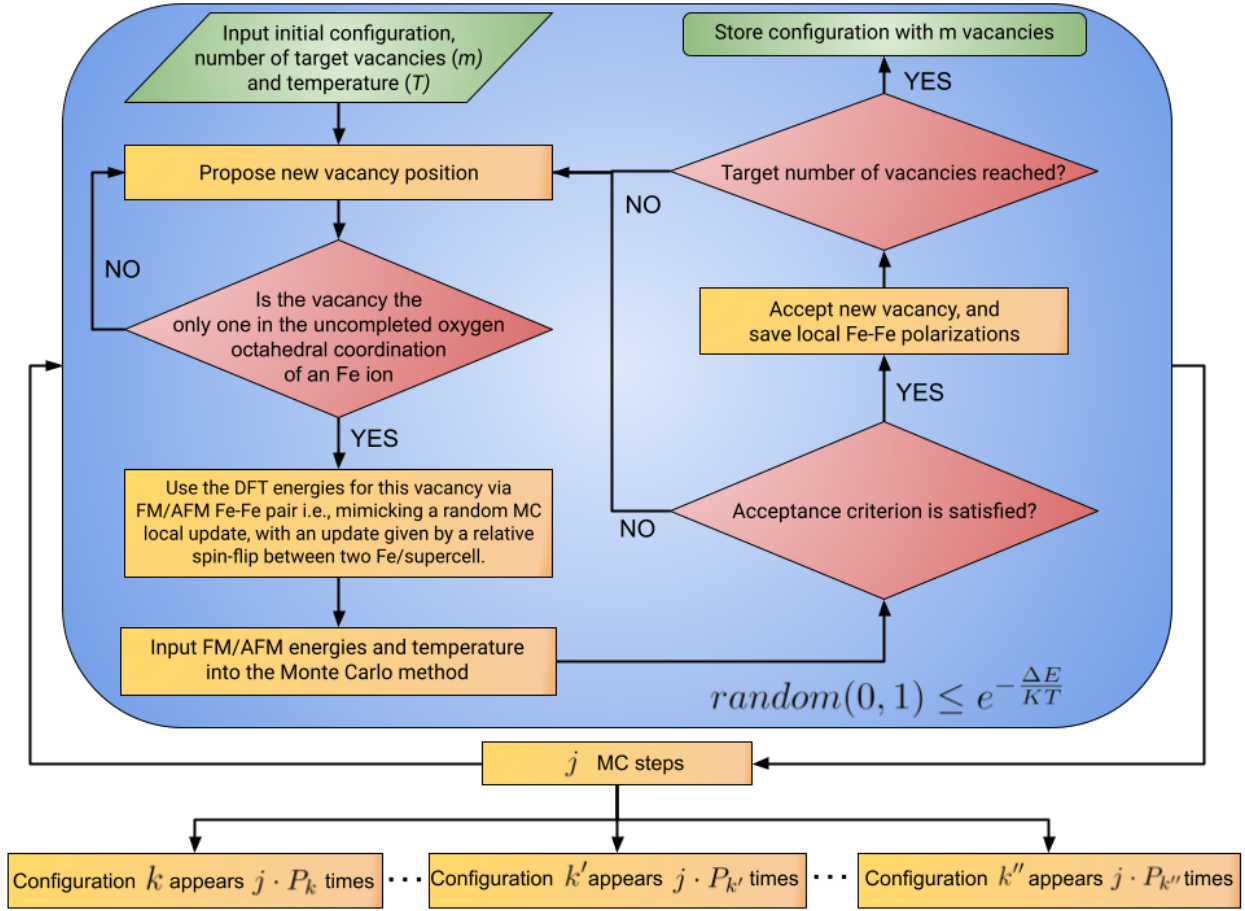


Figure B.10: Diagram of the algorithm used to implement a Metropolis Monte Carlo scheme, which generates effective magnetic sites out of pairs of Fe ions constrained by uncompleted coordinating oxygen-octahedra. Such effective magnetic moments are averaged for every possible vacancy distribution to then calculate the spontaneous perovskite magnetization by using the probabilities of occurrence P_k of such distributions along with their configurational magnetization M_k , through Equation 1.

References

References

- [1] G. Rijnders and D. H. A. Blank, *Nature* 433, 369 EP (2005).
- [2] J. Wang, J. B. Neaton, H. Zheng, V. Nagarajan, S. B. Ogale, B. Liu, D. Viehland, V. Vaithyanathan, D. G. Schlom, U. V. Waghmare, N. A. Spaldin, K. M. Rabe, M. Wuttig, and R. Ramesh, *Science* 299, 1719 (2003).
- [3] K. J. Choi, M. Biegalski, Y. L. Li, A. Sharan, J. Schubert, R. Uecker, P. Reiche, Y. B. Chen, X. Q. Pan, V. Gopalan, L.-Q. Chen, D. G. Schlom, and C. B. Eom, *Science* 306, 1005 (2004).
- [4] H. W. Jang, A. Kumar, S. Denev, M. D. Biegalski, P. Maksymovych, C. W. Bark, C. T. Nelson, C. M. Folkman, S. H. Baek, N. Balke, C. M. Brooks, D. A. Tenne, D. G. Schlom, L. Q. Chen, X. Q. Pan, S. V. Kalinin, V. Gopalan, and C. B. Eom, *Phys. Rev. Lett.* 104, 197601 (2010).
- [5] A. Stucky, G. W. Scheerer, Z. Ren, D. Jaccard, J.M. Poumirol, C. Barreateau, E. Giannini, and D. van der Marel, *Scientific Reports* 6, 37582 EP (2016).
- [6] J. F. Schooley, W. R. Hosler, and M. L. Cohen, *Phys. Rev. Lett.* 12, 474 (1964).
- [7] N. Reyren, S. Thiel, A. D. Caviglia, L. F. Kourkoutis, G. Hammerl, C. Richter, C. W. Schneider, T. Kopp, A.S. Raetschi, D. Jaccard, M. Gabay, D. A. Muller, J.M. Triscone, and J. Mannhart, *Science* 317, 1196 (2007).

- [8] Miyoung Kim, Gerd Duscher, Nigel D. Browning, Karl Sohlberg, Sokrates T. Pantelides, and Stephen J. Pennycook, *Phys. Rev. Lett.* 86, 4056 4059 (2001).
- [9] M. Fiebig, T. Lottermoser, D. Meier, and M. Trassin, *Nature Reviews Materials* 1, 16046 (2016).
- [10] T. Goto, D. H. Kim, X. Sun, M. C. Onbasli, J. M. Florez, S. P. Ong, P. Vargas, K. Ackland, P. Stamenov, N. M. Aimon, M. Inoue, H. L. Tuller, G. F. Dionne, J. M. Coey, and C. A. Ross, *Phys. Rev. Applied* 7, 024006 (2017).
- [11] S. Song, H. Han, H. M. Jang, Y. T. Kim, N.-S. Lee, C. G. Park, J. R. Kim, T. W. Noh, and J. F. Scott, *Advanced Materials* 28, 7430 (2016).
- [12] M. Itoh, R. Wang, Y. Inaguma, T. Yamaguchi, Y.-J. Shan, and T. Nakamura, *Phys. Rev. Lett.* 82, 3540 (1999).
- [13] M. Choi, F. Oba, Y. Kumagai, and I. Tanaka, *Advanced Materials* 25, 86 (2013).
- [14] C. Mitra, C. Lin, A. B. Posadas, and A. A. Demkov, *Phys. Rev. B* 90, 125130 (2014).
- [15] K. Klyukin and V. Alexandrov, *Phys. Rev. B* 95, 035301 (2017).
- [16] A. Lopez-Bezanilla, P. Ganesh, and P. B. Littlewood, *APL Materials* 3, 100701 (2015).
- [17] A. Cammarata and J.M. Rondinelli, *Applied Physics Letters* 108, 213109 (2016).
- [18] Brovko, O. O., and Tosatti, E., *Physical Review Materials*, 1(4), 0444058 (2017).
- [19] F. El-Mellouhi, E. N. Brothers, M. J. Lucero, and G. E. Scuseria, *Phys. Rev. B* 84, 199907 (2011).
- [20] Pai, Y.-Y., Tylan-Tyler, A., Irvin, P., and Levy, J., *Reports on Progress in Physics*, 81(3), 03650 (2018).
- [21] Y. Zhang, J. Wang, M. Sahoo, T. Shimada, and T. Kitamura, *Phys. Chem. Chem. Phys.* 17, 27136 (2015).
- [22] C. Lin, C. Mitra, and A. A. Demkov, *Phys. Rev. B* 86, 161102 (2012).
- [23] J. R. Petrie, C. Mitra, H. Jeon, W. S. Choi, T. L. Meyer, F. A. Reboredo, J. W. Freeland, G. Eres, and H. N. Lee, *Advanced Functional Materials* 26, 1564 (2016).
- [24] Dong, X.-L., Zhang, K.-H., and Xu, M.-X., *Frontiers of Physics*, 13(5), 1155037 (2018).
- [25] Lee, D., Wang, H., Noesges, B. A., Asel, T. J., Pan, J., Lee, J. W., et al., *Physical Review Materials*, 2(6), 060403 (2018).
- [26] Sikam, P., Moontragoon, P., Sararat, C., Karaphun, A., Swatsitang, E., Pinitsoontorn, S., and Thongbai, P., *Applied Surface Science*, 446, 92113 (2018).
- [27] Wang, Y.-G., Tang, X.-G., Liu, Q.-X., Jiang, Y.-P., and Jiang, L.-L., *Nanomaterials*, 7(9), 26412 (2017).
- [28] Zhang, Y., Kurt, O., Ascienzo, D., Yang, Q., Le, T., Greenbaum, S., et al., *Journal of Physical Chemistry C*, 122(24), 12864 12868 (2018).
- [29] Dionne, G. F., New York: Springer, (2009).
- [30] D. H. Kim, N. M. Aimon, L. Bi, J. M. Florez, G. F. Dionne, and C. A. Ross, *Journal of Physics: Condensed Matter* 25, 026002 (2013).
- [31] J. M. Florez, S. P. Ong, M. C. Onbsli, G. F. Dionne, P. Vargas, G. Ceder, and C. A. Ross, *Applied Physics Letters* 100, 252904 (2012).
- [32] A. Walsh, A. A. Sokol, J. Buckeridge, D. O. Scanlon, and C. R. A. Catlow, *The Journal of Physical Chemistry Letters* 8, 2074 (2017).
- [33] M. A. Opazo, S. P. Ong, P. Vargas, C. A. Ross, and J. M. Florez, *Phys. Rev. Mater.*, 3, 014404 (2019).
- [34] Cortés Estay, E. A., Ong, S. P., Ross, C. A., Florez, J. M., *Magnetochemistry*, 8(11), 144, (2022).
- [35] Y. Pai, A. Tylan-Tyler, P. Irvin, and J. Levy, *Rep. Prog. Phys.* 81, 036503 (2018).
- [36] U. Aschauer and N. A. Spaldin, *J. Phys.: Condens. Matter* 26, 122203 (2014).
- [37] Y. S. Kim, J. Kim, S. J. Moon, W. S. Choi, Y. J. Chang, J.-G. Yoon, J. Yu, J.-S. Chung, and T. W. Noh, *Appl. Phys. Lett.* 94, 202906 (2009).
- [38] M. Choi, F. Oba, and I. Tanaka, *Phys. Rev. Lett.* 103, 185502 (2009).
- [39] K. Klyukin and V. Alexandrov, *Phys. Rev. B* 95, 035301 (2017).
- [40] F. Yang, Q. Zhang, Z. Yang, J. Gu, Y. Liang, W. Li, W. Wang, K. Jin, L. Gu, and J. Guo, *Appl. Phys. Lett.* 107, 082904 (2015).
- [41] I. Hallsteinsen, M. Nord, T. Bolstad, P.-E. Vullum, J. E. Boschker, P. Longo, R. Takahashi, R. Holmestad, M. Lippmaa, and T. Tybell, *Cryst. Growth Des.* 16, 2357 (2016).
- [42] I. Sokolovic, M. Schmid, U. Diebold, and M. Setvin, *Phys. Rev. Mater.* 3, 034407 (2019).
- [43] El-Naser, A. A. et al, *Philos Mag* 101, 1–19 (2020).
- [44] X. Wang, Z. Wang, Q. Hu, C. Zhang, D. Wang, and L. Li, *Solid State Commun.* 289, 22 (2019).
- [45] A. S Tang, M. C. Onbasli, X. Sun, and C. A. Ross, *ACS Appl. Mater. Interfaces*, 10, 7469 (2018).
- [46] D. H. Kim, L. Bi, P. Jiang, G. F. Dionne, and C. A. Ross, *Phys. Rev. B* 84, 014416 (2011).
- [47] L. Bi, H.-S. Kim, G. F. Dionne, and C. A. Ross, *New Journal of Physics* 12, 043044 (2010).
- [48] A. B. Posadas, C. Mitra, C. Lin, A. Dhamdhere, D. J. Smith, M. Tsoi, and A. A. Demkov, *Phys. Rev. B* 87, 144422 (2013).
- [49] G. Kresse and J. Furthmuller, *Phys. Rev. B* 54, 11169 (1996).
- [50] G. Makov and M. C. Payne, *Phys. Rev. B* 51, 4014 (1995).
- [51] J. Heyd, G. E. Scuseria, and M. Ernzerhof, *The Journal of Chemical Physics* 124, 219906 (2006).
- [52] Dudarev, S. L., Botton, G. A., Savrasov, S. Y., Humphreys, C. J., Sutton, *Physical Review B*, 57(3), 1505 (1998).
- [53] S. P. Ong, W. D. Richards, A. Jain, G. Hautier, M. Kocher, S. Cholia, D. Gunter, V. L. Chevrier, K. A. Persson, and G. Ceder, *Computational Materials Science* 68, 314 (2013).
- [54] A. Jain, S. P. Ong, G. Hautier, W. Chen, W. D. Richards, S. Dacek, S. Cholia, D. Gunter, D. Skinner, G. Ceder, and K. a. Persson, *APL Materials* 1, 011002 (2013).
- [55] Stokes, H. T., Hatch, D. M., *Journal of Applied Crystallography*, 38(1), 237-238, (2005).
- [56] Reyntjens, Peter D., et al., *Materials* 14.15 (2021).
- [57] Zhurkin, E. E., et al., *Nuclear Instruments and Methods in Physics Research Section B: Beam Interactions with Materials*

- and Atoms 269.14 (2011).
- [58] Shiiba, Hiromasa, et al., *Physical Chemistry Chemical Physics* 15.25 (2013).
 - [59] Hong Ding, Shyam S. Dwaraknath, Lauren Garten, Paul Ndione, David Ginley, and Kristin A. Persson *ACS Applied Materials & Interfaces*, 8 (20), 13086-13093 2016.
 - [60] Horton, M.K., Montoya, J.H., Liu, M. et al., *npj Comput Mater* 5, 64 (2019).
 - [61] Kuhn, M., Kim, J. J., Bishop, S. R. and Tuller, H. L., *Chemistry Of Materials* 25, 2970–2975 (2013).
 - [62] J.M. Florez, J. Mazo-Zuluaga, and J. Restrepo. *Hyperfine Interact*, 161(1), 161-169 (2005).
 - [63] Aramburu, J. A. and Moreno, M., *J Phys Chem* 125, 2284–2293 (2021).
 - [64] J. M. Florez, M. C. Onbasli, D. H. Kim, S. P. Ong, G. Ceder, P. Vargias, and C. A. Ross, Abstract: M32.00014, APS March Meeting 2015, Volume 60, Number 1 (2015).
 - [65] Tahini, H.A.; Tan, X.; Schwingenschlögl, U.; Smith, S.C. *ACS Catal.* 2016, 6, 5565
 - [66] Alexander Stukowski *Modelling Simul. Mater. Sci. Eng.* 18 015012 (2010).
 - [67] H. Raebiger, S. Lany, and A. Zunger, *Nature* 453, 763 (2008).
 - [68] G. M. Dalpian, Q. Liu, C. C. Stoumpos, A. P. Douvalis, M. Balasubramanian, M. G. Kanatzidis, and A. Zunger, *Phys. Rev. Materials* 1, 025401 (2017).
 - [69] Varignon, J., Grisolia, M. N., Iniguez, J., Barthelemy, A., and Bibes, M. (2017). *Npj Quantum Materials*, 2(1), 21.
 - [70] Yan, B., Jansen, M., and Felser, C., *Nature Physics*, 9(11), 709 (2013).
 - [71] Kim, N., Perry, N. H., Ertekin, E., *Chemistry of Materials*, 31(1), 233–243(2018).
 - [72] Bin Ouyang, Chakraborty, T., Kim, N., Perry, N. H., Mueller, T., Aluru, N. R., Ertekin, E., *Chemistry of Materials*, (2019).
 - [73] Xu, T., Shimada, T., Araki, Y., Wang, J. & Kitamura, T, *Nano Letters* 16, 454–458 (2015).
 - [74] Lee, Kyoungjun, et al., *Scientific reports* 11.1, 1-9 (2021).
 - [75] Cheng, S. et al. *Adv Funct Mater* 26, 3589–3598 (2016).
 - [76] Allen, Jeremy P., and Graeme W. Watson., *Physical Chemistry Chemical Physics* 16.39, 21016-21031, (2014).